Chemical Engineering Journal 498 (2024) 155117

Contents lists available at ScienceDirect

Chemical Engineering Journal

journal homepage: www.elsevier.com/locate/cej

Vacancies engineering in ultrathin porous g-C_3N_4 tubes for enhanced photocatalytic PMS activation for imidacloprid degradation

Bin Yang [a,1], Jiaojiao Zhao [a,1], Youpeng Xiong [a], Cuihua Li [a,*], Mei Zhang [a], Raul D. Rodriguez [b,*], Xin Jia [a,*]

[a] School of Chemistry and Chemical Engineering/State Key Laboratory Incubation Base for Green Processing of Chemical Engineering, Shihezi University, Shihezi 832003, China

[b] Tomsk Polytechnic University, 30 Lenin Avenue, 634050 Tomsk, Russia

ARTICLE INFO

Keywords:
Photocatalysis
Carbon nitride
Vacancies and morphology
Peroxymonosulfate
Degradation

ABSTRACT

Precise morphology and vacancy engineering is a promising strategy to enhance the degradation performance of refractory contaminants in photocatalysis coupling peroxymonosulfate activation (PC-PMS) systems. In this context, we developed ultrathin porous g-C_3N_4 tubes with three-coordinated nitrogen (N_b) vacancies between the heptazine units through hydrogen intercalated exfoliation and selective nitrogen removal at high temperatures. The ultrathin porous tubular architecture provides an ultrahigh-specific surface area with abundant exposed active sites, ensures effective mass transfer, and shortens the diffusion distance of photogenerated carriers. The N_b vacancies act as unsaturated sites, inhibiting the photogenerated carrier's recombination and facilitating the adsorption/activation of O_2 and its conversion to $\bullet O_2^-$ via photogenerated electrons. Then, the PMS is subsequently oxidated by photogenerated holes selectively producing $^1O_2$. Together, these continuously released free radicals unlock the complete degradation of imidacloprid within 20 min in the PC-PMS system, with a degradation rate about 350 % higher than conventional g-C_3N_4 tubes and 10-fold that of pristine g-C_3N_4. This study provides a novel insight into the efficient utilization of photogenerated electron-hole pairs conversion to $\bullet O_2^-$ and $^1O_2$ for the removal of pesticide contaminants through the rational design of photocatalysts in the PC-PMS system.

1. Introduction

As a member of neonicotinoid insecticides, imidacloprid (IMD) is the world's most widely used and fastest-developing insecticide due to advantages such as strong persistence, high neurotoxicity, and excellent selective action mechanism. Nevertheless, due to the low utilization rate, long half-life in soil, and high solubility in water, IMD widely persists in nature after it has performed its intended pesticide role [1]. IMD sub-lethal toxicity for non-target organisms can lead to reduced growth and reproductive rates, impaired immune function, damage to the nervous system, disturbances in metabolic balance, and DNA damage. Those issues directly threaten non-target organisms, the environment, and human health [2,3]. Therefore, the efficient removal of IMD is essential. Photocatalysis has the potential for application in pollutant removal due to its low energy consumption and mild reaction conditions [4]. However, its efficiency is greatly limited by the serious recombination of photogenerated charges. In this context, the photocatalysis coupling peroxymonosulfate activation (PC-PMS) system is promising for removing refractory pollutants like IMD [5–8]. The addition of PMS can effectively promote the separation of photogenerated charges and be further activated to produce highly active free radicals that degrade pollutants efficiently [9]. One of the main challenges nowadays is to select and optimize photocatalysts to improve the synergistic effect between PMS activation and photocatalysis.

Graphitic carbon nitride (g-C_3N_4) is a promising PMS activator for the degradation of refractory pollutants due to advantages such as rich material sources, stable physicochemical properties, adjustable structure, and easy preparation [10,11]. However, the photocatalytic activity of pristine g-C_3N_4 has been commonly limited by insufficiently low density of exposed active sites, high recombination of photogenerated carriers, and poor adsorption/activation ability for O_2 and PMS. Fortunately, the modification of g-C_3N_4 is easy to implement and can be

* Corresponding authors.
E-mail addresses: lich@shzu.edu.cn (C. Li), raul@tpu.ru (R.D. Rodriguez), jiaxin@shzu.edu.cn (X. Jia).
[1] These authors contributed equally to this work.

https://doi.org/10.1016/j.cej.2024.155117
Received 8 June 2024; Received in revised form 20 August 2024; Accepted 22 August 2024

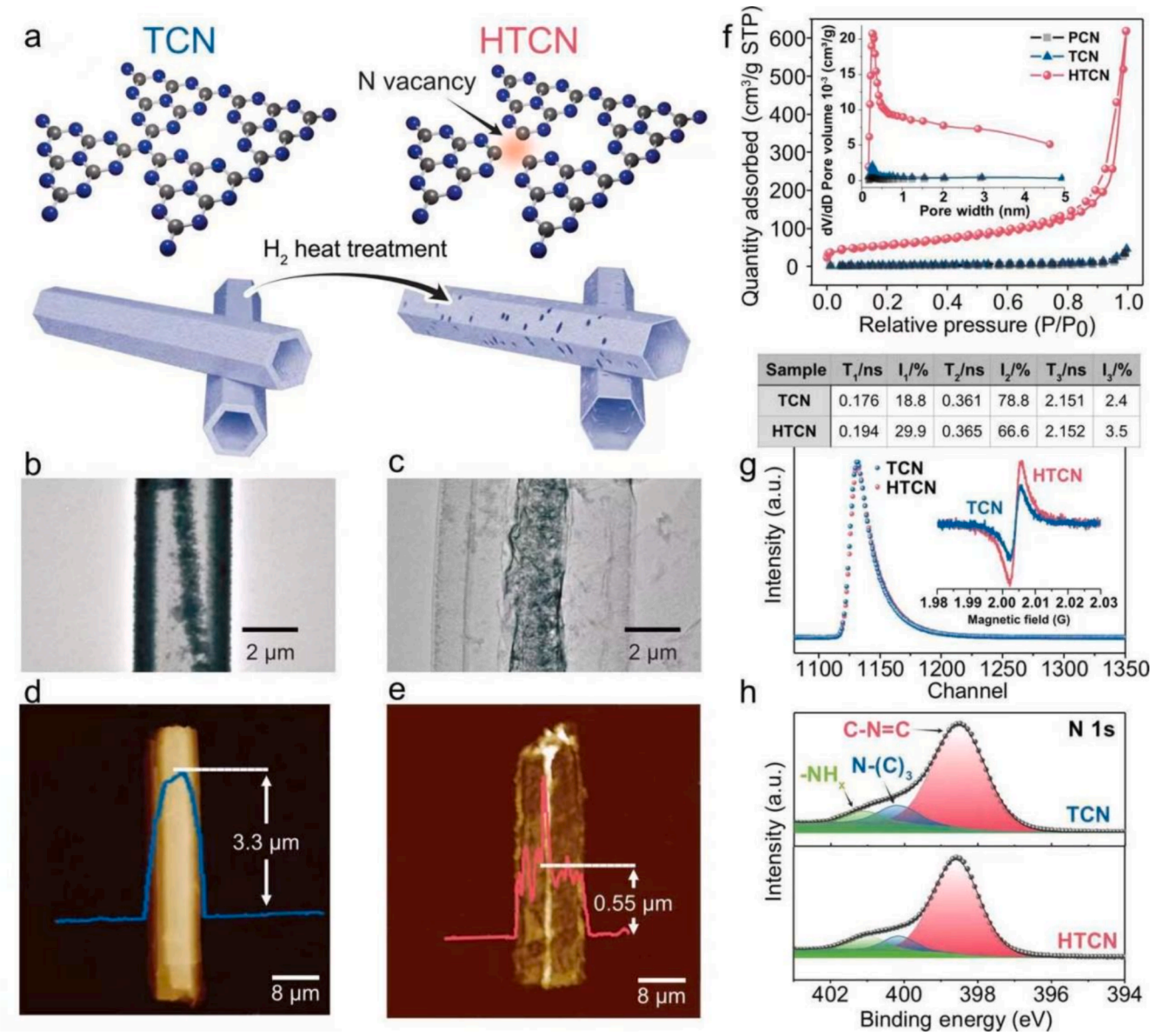

Sample	T_1/ns	I_1/%	T_2/ns	I_2/%	T_3/ns	I_3/%
TCN	0.176	18.8	0.361	78.8	2.151	2.4
HTCN	0.194	29.9	0.365	66.6	2.152	3.5

Fig. 1. Schematic illustration of the prepared route of HTCN (a); TEM images of TCN (b) and HTCN (c); AFM imaging corresponding height profiles of TCN (d) and HTCN (e); Specific surface area (Inlaying pore size distribution) (f), Positron annihilation spectra (Inlaying EPR spectra) (g), N 1 s XPS spectra (h) of TCN and HTCN.

further optimized to improve its photocatalytic activity [12]. Therefore, many strategies are being explored to improve g-C_3N_4 photocatalytic performance, such as vacancy engineering [13], element doping [14], heterojunction construction [15,16], morphology design [17], etc. Among the multiple modification strategies, the simultaneous precise engineering of morphology and vacancies is an exciting avenue to improve photocatalytic activity.

Compared with two-dimensional nanosheets, three-dimensional g-C_3N_4 tubes prepared by supramolecular self-assembly exhibit much higher photocatalytic performance, owing to improved characteristics such as intense light scattering ability, quantum confinement effects and enhanced electron-directed transfer channels [18]. However, pushing this alternative forward is limited by the thick tube wall that affects the photocatalytic activity of g-C_3N_4 [19–21]. Ultrathin porous tubes can provide a larger specific surface area with highly exposed active sites and a shorter diffusion path for photogenerated carriers. Hence, the engineering exfoliation for preparing ultrathin porous g-C_3N_4 tubes will significantly enhance its photocatalytic performance. The vacancies are another important approach to boosting photocatalytic performance effectively [22,23]. Specifically, the two-coordinated nitrogen (N_i) vacancies in the heptazine units can accelerate the migration of photogenerated carriers, serving as sufficient reaction sites to boost the adsorption and activation of the reaction medium [24–26]. Compared to the above N_i vacancies, the three-coordinated nitrogen (N_b) vacancies between the heptazine units cause more significant symmetry breaking [27], and possess more abundant lone pair electrons, which promote the generation of richer photogenerated carriers [28]. However, the N_b vacancies are rarely reported due to challenges associated with high formation energy. The important role of accurately constructed N_b vacancies in optimizing its photocatalytic activity is necessary for deeply exploration. Motivated by the above discussion, it is conceivable that the creative construction of ultrathin porous g-C_3N_4 tubes with N_b vacancies will significantly improve the synergistic effect between PMS activation and photocatalysis, supporting excellent degradation properties.

Herein, we creatively synthesized ultrathin porous g-C_3N_4 tubes with N_b vacancies (HTCN) by hydrogen gas (H_2)-assistant heat treatment (see to Fig. 1a). Both experimental and theoretical results demonstrate that H_2 molecules can diffuse into the interlayer of g-C_3N_4 tubes and tend to

precisely adsorb on the three-coordinated nitrogen atoms between the heptazine rings. At high temperatures, H_2 molecules react with these nitrogen atoms to produce N_b vacancies. The NH_3 and H_2O gases *in situ* generated during the reaction induce the stripping and piercing of g-C_3N_4 tubes. Morphological and structural observations confirm that ultrathin porous g-C_3N_4 tubes were successfully obtained. Multiple characterization analyses points to the successful introduction of N_b vacancies in g-C_3N_4 frameworks. We found that our HTCN material exhibits a very high specific surface area with rich exposed active sites and efficient separation of photogenerated carriers. As a result, the HTCN photocatalyst could entirely degrade IMD within 20 min in the PC-PMS system, with a degradation rate about 10 and 3.5 times higher than that of pristine g-C_3N_4 and g-C_3N_4 tubes, respectively. Different conditions and their roles in the degradation of IMD were investigated, such as water matrices, pH values, and co-existing ions. A possible degradation mechanism involving $\bullet O_2^-$ and $^1O_2$ is proposed based on free radical quenching experiments and electron spin resonance data. This work provides a novel approach and insights for constructing highly efficient photocatalysts via morphology control and vacancy engineering to remove pesticide contaminants.

2. Experimental section

2.1. Synthesis of PCN

The pristine g-C_3N_4 was synthesized as follows: 5 g melamine was placed in a covered ceramic crucible and then calcined at 550℃ at 5℃/min heating rate for 4 h in a muffle furnace under static air. The yellow product was denoted as PCN.

2.2. Synthesis of TCN

The hexagonal prismatic precursor was obtained through precise supramolecular pre-assembly of melamine and cyanuric acid and then calcined in an N_2 atmosphere to obtain pristine g-C_3N_4 tubes. The detailed preparation process is as follows: 1 g of melamine was dispersed into 60 mL water after completely dissolving at 90℃ and then transferred to a Teflon reactor to react at 200℃ for 12 h. The hexagonal prismatic crystal composed of melamine and cyanic acid was obtained through natural cooling, centrifugation, and drying. Under the protection of nitrogen gas, the tube furnace containing 1g precursor was heated to 550℃ at a heating rate of 5℃ min^{-1} and then calcined at this temperature for 2 h. After cooling to room temperature, the obtained yellow powders are g-C_3N_4 tubes labeled as TCN.

2.3. Synthesis of HTCN

Well-controlled H_2-assisted thermal treatment was used to synthesize ultrathin porous g-C_3N_4 tubes with modulated N_b vacancies, achieving the precise regulation of the morphology and vacancy. The detailed preparation process is as follows: 0.2 g of TCN powders in a quartz crucible were placed in the center of the tube furnace and heated at 550 °C under an H_2 gas atmosphere for 60 min with a heat rate of 5 °C min^{-1}. After cooling to room temperature, the obtained white powders were ultrathin porous g-C_3N_4 tubes modified with N_b vacancies labeled HTCN.

In brief, the synthesis process of HTCN has the potential to be scaled up, considering that H_2 gas as a reactant and its products have less negative impact on the environment, while the prepared g-C_3N_4 is mainly derived from low-cost urea.

2.4. Photocatalytic performance assessment

Based on the flexibility of wavelength and light intensity and the stability of output energy, a 300 W xenon lamp ($\lambda \geq 420$ nm cut-off filter) was used as the light source to simulate sunlight for IMD's degradation in the PC-PMS system and explore the relationship between catalyst activity and structure. 20 mg of photocatalyst was added to a jacketed beator containing 50 mL of IMD (10 ppm) solution. Stirring in the dark for 30 min to achieve absorption–desorption equilibrium between the photocatalyst and IMD molecules. The light was turned on immediately when 2 mM of PMS was added to the system. The IMD degradation process was kept under 25℃ with circulating water to maintain the degradation environment constant and minimize the impact of thermal effects. Samples were taken at fixed intervals during photocatalytic degradation of IMD. The solution was separated from the photocatalyst by centrifugation at 10000 rpm. The supernatant was filtered with a 0.22 μm polytetrafluoroethylene filter. The concentration of IMD solution was determined by High-performance liquid chromatography. The photocatalysis (PC) system is similar to a PC-PMS, except without adding PMS. The steps of the degradation experiment by cycling were as follows: after the first degradation experiment, the sample (HTCN) was separated, filtered with distilled water, washed, and then subjected to the next degradation experiment for ten cycles.

2.5. Continuous flow experiments

The schematic of the custom-made photo-flow device is presented in Fig. S18. The flow reactor comprised quartz tubes 20 cm in length, 2 cm in diameter, and 0.1 cm in wall thickness. The quartz tube was packed with 100 mg of HCN photocatalyst, and both ends consisted of two layers of 4.5 μm filter membrane of 1.5 cm diameter with 0.5 cm thick cotton sandwiched between the filter membrane, thus guaranteeing that the HCN could be stabilized inside the tube without loss. Outdoor sunlight was used to irradiate this reactor, while a peristaltic pump provided a flow rate of 12 mL/h of 10 ppm IMD solution. The concentration of IMD was measured by taking a liquid every 2 h from 10 am to 10 pm on July 26–28 in Shihezi, Xinjiang.

2.6. Characterization

Powder X-ray diffraction (XRD) measurements were collected on a Rigaku D/MAX-RB diffractometer with monochromatic Cu Kα radiation ($\lambda = 0.15418$ nm). X-ray photoelectron spectra (XPS) were detected using a Thermo Scientific K-Alpha spectrometer using a standard Al Kα X-ray source (hv = 1486.6 eV). Scanning electron microscopy (SEM) images were recorded on a Hitachi SU8010 instrument. Transmission electron microscopy (TEM) images were recorded on a Hitachi HT7700 electron microscope. An atomic force microscope (AFM) Bruker Multimode 8 was used to acquire surface topography images. The reflectance spectra of all samples over the 190–1000 nm range were obtained by A UV–visible spectrometer equipped with a Labsphere diffuse reflectance accessory (UV-2550, Shimadzu, Japan), using $BaSO_4$ as the reference standard. Fourier transform infrared (FTIR) patterns were collected on a Bruker Vertex 70 V spectrometer over the frequency range 4000–400 cm^{-1} at a resolution of 2 cm^{-1}. All samples' specific surface area analysis was obtained using an N_2 adsorption–desorption instrument (BET, ASAP2020, USA). ^{13}C magic angle spinning (MAS) NMR measurements were acquired on a Bruker AVANCE III 400 MHz WB solid-state NMR spectrometer. The photoluminescence (PL) and time-resolved PL (TRPL) spectra were recorded using an Edinburgh FLS1000 spectrophotometer. An organic element analyzer was acquired on an Elementar Vario EL cube, Germany.

The following is described in detail in the supplementary information: Material and reagent, photoelectrochemical measurement, photocatalytic hydrogen evolution and computation.

3. Results and discussion

3.1. Morphology characterization

The micro-morphology of the samples was analyzed by TEM,

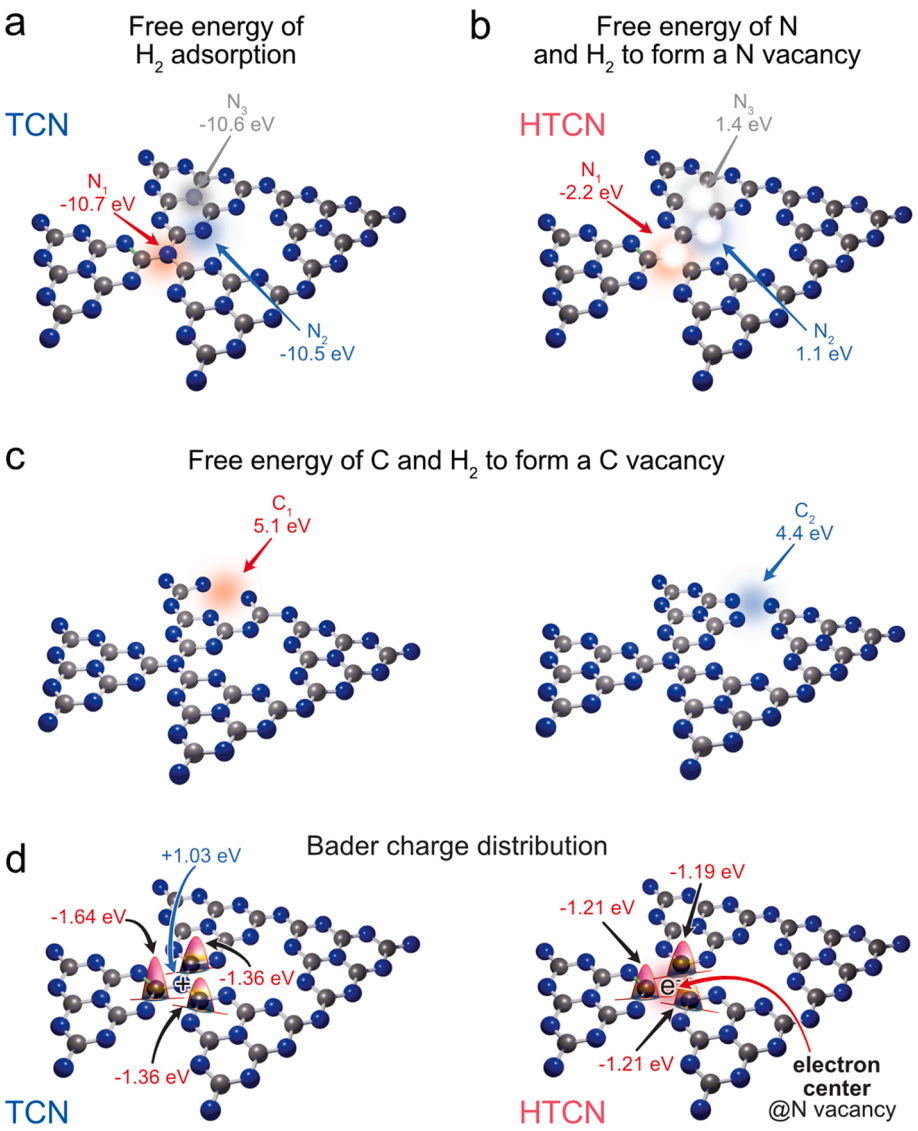

Fig. 2. (a) The free energy of adsorption of H_2 molecules adsorbed on different nitrogen atoms; (b) The free energy of the reaction between nitrogen atoms and H_2 molecules to form a nitrogen vacancy; (c) The free energy of the reaction between the carbon atoms and hydrogen molecules to form carbon vacancies; (d) Structure and Bader charge analysis of TCN and HTCN, respectively.

showing that both HTCN and TCN present hollow tubes, as depicted in Fig. 1b and 1c. Note the thick tube wall that the conventional TCN obtained by calcination shows. In contrast, the HTCN has an ultra-thin tubular structure. These results were confirmed by 3D imaging with AFM, showing that the vertical height of TCN is 3.3 μm, see Fig. 1d. In comparison, the vertical height of HTCN is only 0.55 μm (Fig. 1e), suggesting that HTCN maintains its tubular structure after H_2 heat treatment. In contrast, HTNC's vertical height is significantly lower than that of TCN due to the thinning of the tube wall. SEM results in Fig. S1 also show similar morphological characteristics. However, the length and diameter of the HTCN could not be standardized (Fig. S1c) due to the inherent temperature instabilities of the precursor during the cooling and crystallization process [29]. In addition, the g-C_3N_4 tubes tend to fracture during the calcination process. These observations demonstrate that g-C_3N_4 ultra-thin tubes can be obtained by hydrogen heat treatment. BET results show that HTCN has the highest specific surface area (192.33 m^2g^{-1}) among all samples, about 14 and 27 times that of TCN and PCN, respectively (Fig. 1f). HTCN also presents a fluffier and larger volume at the same mass compared with PCN and TCN (Fig. S2). Fig. 1f shows the pore size distribution curve of the catalysts. We attribute the remarkable average pore size increase of HTCN to the thinner wall of g-C_3N_4 tubes after H_2 heat treatment. Consequently, the significant increase of specific surface area and microporous structure in HTCN is more conducive to promoting adsorption and activation of reactants.

3.2. *Characterization of N_b vacancies*

The EPR spectra were performed to investigate samples' vacancies [30] (Fig. 1g). TCN and HTCN exhibit clear EPR signals at a g value of 2.004, corresponding to the local unpaired electrons around the vacancies in g-C_3N_4. The stronger EPR intensity in HTCN indicates that more vacancies are formed after the hydrogen heat treatment. The type of vacancies formed was further elucidated by organic element analysis. The C/N ratio of TCN and HTCN is 0.604 and 0.616, respectively. The significant reduction of nitrogen content directly points to the introduction of nitrogen vacancies in HTCN after H_2 heat treatment. These analyses prove that H_2 heat treatment can introduce nitrogen vacancies into the HTCN framework.

Positron annihilation spectra (PAS) can provide information on the size, type, and relative concentration of various vacancies depending on the positron's lifetime [31]. Therefore, PAS was used to analyze the distribution of nitrogen vacancies. PAS analysis results of TCN and

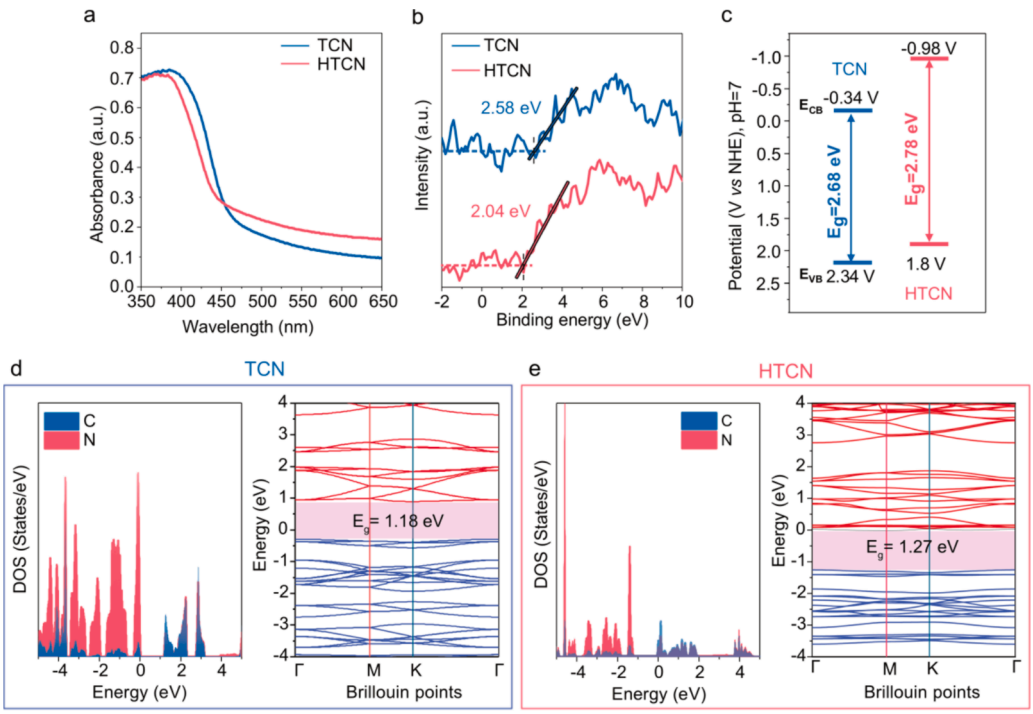

Fig. 3. (a) UV–Vis diffuse reflectance spectra, (b) VB-XPS spectra, (c) Schematic band structures of TCN and HTCN; Density of states and corresponding band structures of (d) TCN and (e) HTCN.

HTCN in Fig. 1g include the three positron lifetime components (τ_1, τ_2, and τ_3) and their relative intensities (I_1, I_2, and I_3). The shortest lifetime of τ_1 is denoted as the first lifetime of positrons, which usually depends on the free annihilation of positrons in a vacancies-free crystal. In a disordered system, smaller vacancies or shallower positron traps may reduce the surrounding electron density, thereby increasing the lifetime of τ_1. Among them, the τ_1 of TCN is 0.176 ns, which may be attributed to the inherent lifetime of free positron in TCN. In contrast, the τ_1 of HTCN is significantly longer at 0.194 ns than TCN. The increased τ_1 for HTCN indicates that a large number of small-size nitrogen vacancies were introduced into HTCN by H_2 heat treatment. Correspondingly, the relative strength of I_1 in HTCN increases from 18.8 % in TCN to 29.9 % in HTCN. Compared with the lifetime of τ_1, the lifetime of τ_2 is longer due to the positrons trapped by larger size vacancies, where the average electron density is lower than in smaller size vacancies, which correspondingly reduces the annihilation rate and increases the positron lifetime. Compared with TCN (0.361 ns), the τ_2 of HTCN increases to 0.365 ns, indicating that a large size of nitrogen vacancies was generated in HTCN. The slightly higher τ_3 in HTCN is probably due to the annihilation of positron atoms formed in large-size nanopores. In this study, τ_3 was detected in TCN at 2.151 ns, while a longer τ_3 was detected in HTCN at 2.152 ns. Moreover, I_3 in HTCN (3.5 %) was stronger than in TCN (2.4). The results show that relatively more nanopores were introduced into HTCN after H_2 heat treatment, which can provide abundant active sites for the reactants. These PAS results suggest that compared with TCN, not only did the nitrogen vacancies exist in HTCN, but they also present abundant nanopore structures that were beneficial for the catalytic reaction.

The XPS N 1 s spectra of the samples in Fig. 1h were analyzed to further reveal the types of nitrogen vacancies in HTCN and the associated structural changes caused by these vacancies [32]. There are three distinct peaks at 398.5, 400.4, and 401.1 eV, attributed to the di-coordinated sp^2 nitrogen in the heptazine units (C-N=C), the bridged tri-coordinated nitrogen atoms (N-$(C)_3$), and the terminal NH_x groups ($-NH_x$), respectively. The nitrogen content is calculated according to the peak area of different types of nitrogen in the XPS N1s spectra. Compared with TCN (N_{3C}/N_{2C}=0.12), the N_{3C} to N_{2C} ratio of HTCN (N_{3C}/N_{2C} = 0.10) decreases, which indicates that the nitrogen vacancies are mainly located at the N_{3C} sites during H_2 heat treatment. We designate these particular three-coordinated N vacancies as N_b vacancies. Note that the N-$(C)_3$ peak in HTCN shifts slightly towards the lower binding energy (400.1 eV), indicating that the N_b vacancies have a specific effect on the local arrangement of the surrounding atoms.

To prove that H_2 molecules can react with nitrogen atoms in the g-C_3N_4 to produce N_b vacancies during H_2 heat treatment, we calculated by density functional theory (DFT) the adsorption free energy of H_2 molecules adsorbed on each nitrogen atom in the g-C_3N_4 framework. As shown in Fig. 2a, the H_2 molecules adsorbed on the nitrogen atoms at N_1 positions have the lowest required adsorption free energy. This indicates that H_2 molecules are more likely to attach to nitrogen atoms at N_1, which can facilitate the subsequent reaction. As shown in Fig. 2b, the reaction free energy required for each nitrogen atom on the g-C_3N_4 framework to react with H_2 molecules to form a nitrogen vacancy is calculated. The results show that the free energies of H_2 molecules with N_2 and N_3 nitrogen atoms in heptazine units are greater than zero, which means that H_2 molecules cannot spontaneously react at N_2 and N_3 locations. Interestingly, the H_2 molecule reaction free energy at the N_1 position is less than zero, indicating that the nitrogen atoms at the N_1 position spontaneously react with H_2 molecules to form N_b vacancies. This further suggests that the formation of nitrogen vacancies is most likely to occur at N_1 nitrogen atoms. To definitely show that H_2 molecules preferentially react with the nitrogen atoms between heptazine units (forming N_b vacancies) instead of carbon atoms within heptazine units (forming carbon vacancies), we calculated the reaction free energies for the formation of carbon vacancies at the C_1 and C_2 positions reacting with H_2. As shown in Fig. 2c, the required reaction free energy at both locations is > 0 and larger than the negative free energy required to form N_b vacancies. The above analysis implies that H_2 molecules are more likely to adsorb and react with nitrogen atoms to form N_b vacancies within g-C_3N_4 tubes during H_2 heat treatment. These computational results are consistent with XPS analyses.

We expect that the formation of N_b vacancies enables the modulation

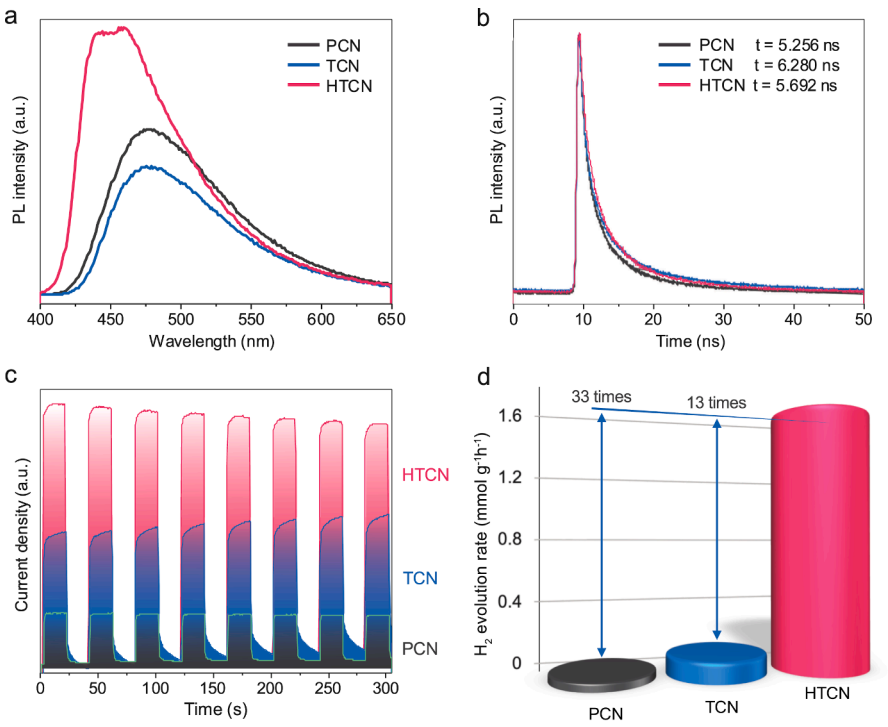

Fig. 4. (a) PL spectra, (b) time-resolved PL decay curves, (c) transient photocurrent responses, and (d) photocatalytic H_2 evolution rate of PCN, TCN, and HTCN.

of the electronic structure. To confirm this, we calculated the Bader charge by DFT calculations that show locally distributed effective charges around the N_b vacancies (Fig. 2d). The charge distribution of adjacent carbon atoms ranges from −1.36, −1.64, and −1.36 eV to −1.20, −1.21, and −1.19 eV, respectively. Residual electrons from the removed nitrogen atom and the reduction electrons on the neighboring carbon atom mainly localize at the N_b vacancy sites, forming an electron center. The N_b vacancies can form electron traps that guide the electrons between the heptazine units to gather around the N_b vacancies and form localized states. These localized states induced by N_b vacancies can promote exciton dissociation and charge separation, critical to enhancing the photocatalytic reaction.

3.3. Optical properties and band structure

The samples' light absorption behavior and band structures were analyzed by UV–vis DRS and XPS valence band (VB-XPS) spectra [33]. The TCN sample exhibits strong light absorption, especially above 450 nm (Fig. 3a). In contrast, the absorption edge of HTCN has a significant blue shift due to the N_b vacancies and quantum confinement effects caused by the ultra-thin structure. In addition, As determined from the transformed Kubelka-Munk function [35], the intrinsic bandgaps of the TCN and HTCN were calculated to be 2.68 and 2.78 eV, respectively (Fig. S6). The increased bandgap of HTCN with H_2 heat treatment is attributed to the synergy of N_b vacancies and quantum confinement effects [34]. The VB-XPS spectra were used to detect the valence band position of the catalysts (Fig. 3b), where the $E_{VB\text{-}XPS}$ of TCN and HTCN were identified as 2.58 and 2.04 eV, respectively. The $E_{VB}=\varphi + E_{VB\text{-}XPS}$-4.44 formula is mainly used to calculate the valence band position (E_{VB}) relative to the standard hydrogen electrode (NHE) at pH=7, where φ represents the work function of the analyzer equal to 4.2 eV[35,36]. Based on the combination of bandgap and E_{VB}, we were able to deduce the band structures of TCN and HTCN shown in Fig. 3c. The higher conduction band value implies that HTCN has a higher reduction potential and stronger reduction ability, which is more conducive to the electron reduction of O_2 on the conduction band to produce $\bullet O_2^-$ radicals.

We calculated the density of states (DOS) of TCN and HTCN using DFT to investigate the relationship between N_b vacancies and the g-C_3N_4 bandgap [35]. These computational results presented in Fig. 3d and 3e show that both C 2p and N 2p orbitals contribute to the CB composition, while the VB is mainly composed of N 2p orbitals. The calculated bandgaps are 1.18 eV and 1.27 eV for TCN and HTCN, respectively. According to the DFT calculation results, introducing N_b vacancies in HTCN can effectively widen the bandgap, consistent with the analysis derived from UV–vis DRS spectra.

3.4. Photogenerated carries' migration behavior

Steady-state PL spectra were recorded to monitor the behavior of photogenerated charges [37]. Compared with PCN, TCN showed a lower steady-state PL intensity due to the tubular morphology of TCN (Fig. 4a). This tube shape can better enhance diffusion and migration of photogenerated charges. However, compared with TCN, the fluorescence intensity of HTCN does not decrease, and the corresponding position of the emission peak is blue-shifted. This phenomenon can be ascribed to the decrease in conjugation length and the strong quantum confinement effect due to the ultrathin porous architecture [38,39]. Furthermore, this observation further reflects that the thick tube wall in TCN undergoing H_2-assisted heat treatment was successfully stripped into an ultra-thin tubular structure. TRPL spectra allowed us to determine the carrier lifetimes of the samples [40]. Compared with TCN, the lifetime value of HTCN decreases from 6.28 ns to 5.69 ns (Fig. 4b). The shortened carrier lifetime is attributed to an effective charge separation derived from N_b vacancies, which is conducive to activating O_2 and PMS. Both photocurrent response and electrochemical impedance spectra were recorded to investigate the photochemical properties of the samples. Compared with PCN and TCN, HTCN exhibits the strongest transient photocurrent response signal (Fig. 4c), as well as the smallest Nyquist radius in the electrochemical impedance diagram (Fig. S7), which is attributed to the synergy of N_b vacancies and ultrathin porous architecture. These observations indicate that HTCN presents the most effective rapid diffusion and migration of photogenerated charges [41]. The utilization efficiency of photogenerated charges that migrated to the catalyst surface was

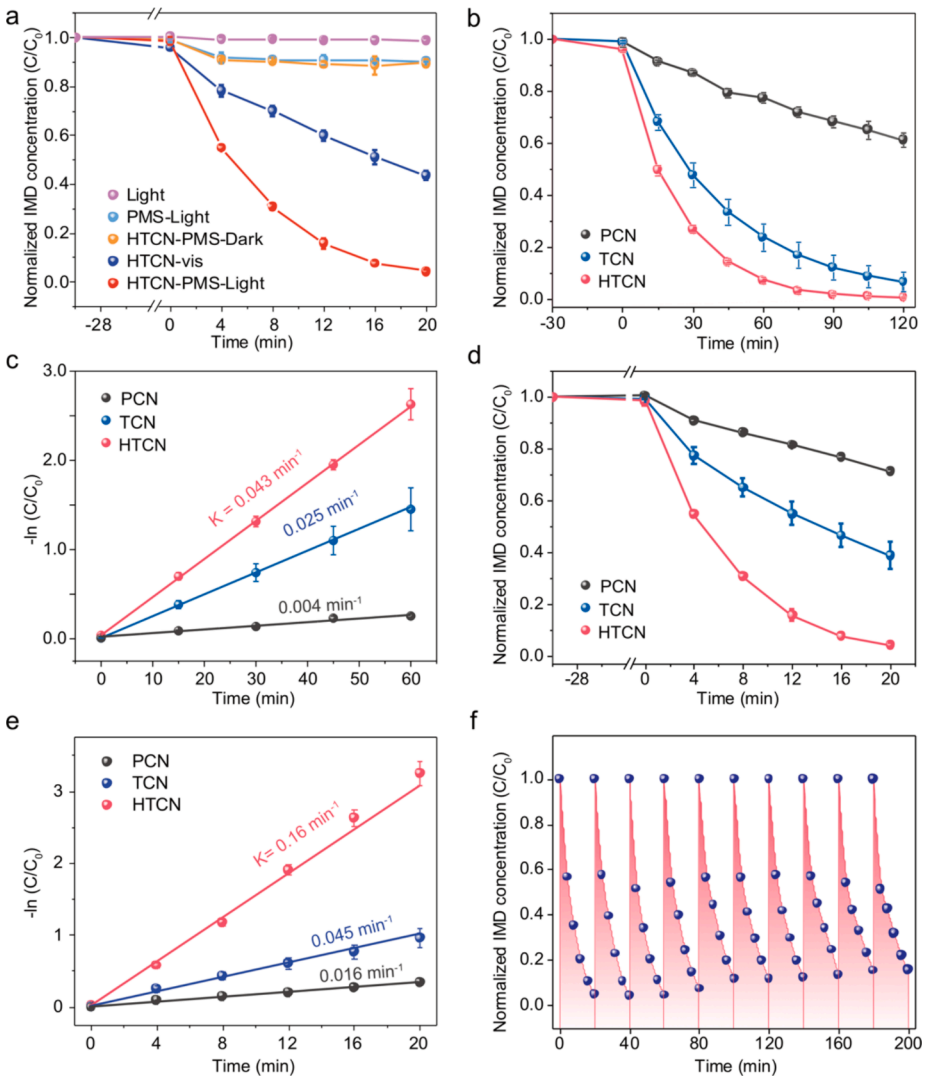

Fig. 5. (a) IMD degradation curves under different conditions; IMD degradation (b, d) and the pseudo-first-order kinetic modeling (c, e) over PCN, TCN, and HTCN in PC system and PC-PMS system, respectively; (f) Cycling stability test of IMD degradation over HTCN in PC-PMS system.

characterized by photocatalytic H_2 evolution. As shown in Fig. 4d and Fig. S7b, the photocatalytic H_2 evolution rate of HTCN is 33 and 13 times that of PCN and TCN under $\lambda \geq 420$ nm visible light, respectively, implying that HTCN has the highest utilization efficiency of photogenerated charges. The above results demonstrate that HTCN presents the best separation, migration, and utilization efficiencies of photogenerated charges, thanks to the synergistic effect of morphology and N_b vacancies.

3.5. IMD degradation performance

As mentioned above, HTCN can be an excellent metal-free catalyst candidate for pesticide degradation in PC-PMS systems. The catalytic activity of HTCN for IMD degradation in the PC-PMS system was examined and compared with PCN and TCN. The degradation of IMD in different conditions was first investigated. Results in Fig. 5a show that IMD degradation does not occur by light exposure alone. In addition, PMS activated solely by light or the catalyst achieved only 10 % degradation in 10 min, with no further IMD concentration change over time. Degradation of IMD can occur only in the presence of the PC or PC-PMS systems under illumination. Various experimental conditions were optimized to obtain the best reaction system, and the optimal doses of IMD, catalyst, and PMS were determined to be 10 ppm, 20 mg, and 2.0 mM, respectively (Fig. S8a-c). HTCN preparation processes were also optimized, showing that the HTCN obtained at 500°C for 60 min has the best performance for IMD degradation (Fig. S9). This temperature appears optimal, likely due to balancing vacancy formation while preserving the structural integrity of HTCN. Under these conditions, HTCN achieved 52 % IMD degradation efficiency within 20 min and complete degradation (100 %) within 90 min in the PC system (Fig. 5b). Simulation results in Fig. 5c show that IMD degradation follows a quasi-first-order kinetics. The reaction rate constant K of HTCN (0.043 min^{-1}) is about 1.7-fold and 11-fold compared to those of TCN (0.025 min^{-1}) and PCN (0.004 min^{-1}), respectively. Meanwhile, in the PC-PMS system, IMD degradation by HTCN reaches 100 % efficiency in 20 min (Fig. 5d). Notably, the reaction rate constant K of HTCN (0.16 min^{-1}) is about 10-fold and 3.5-fold compared to those of TCN (0.045 min^{-1}) and PCN (0.016 min^{-1}), respectively (Fig. 5e). Compared with the PC system, there is a 3.7-fold increase in the IMD degradation rate by the PC-PMS system. These results show that the degradation of IMD originates from the combined effects of photocatalysis and PMS activation. Based on the PMS decomposition experiments, the PMS decomposition efficiency reached 54 % and 66 % for TCN and HTCN in 20 min, respectively (Fig. S10). Moreover, HTCN shows superior IMD degradation in PC-PMS systems compared to the metrics reported in previous studies. Notably, compared to reports in PC systems, the enhancement of the

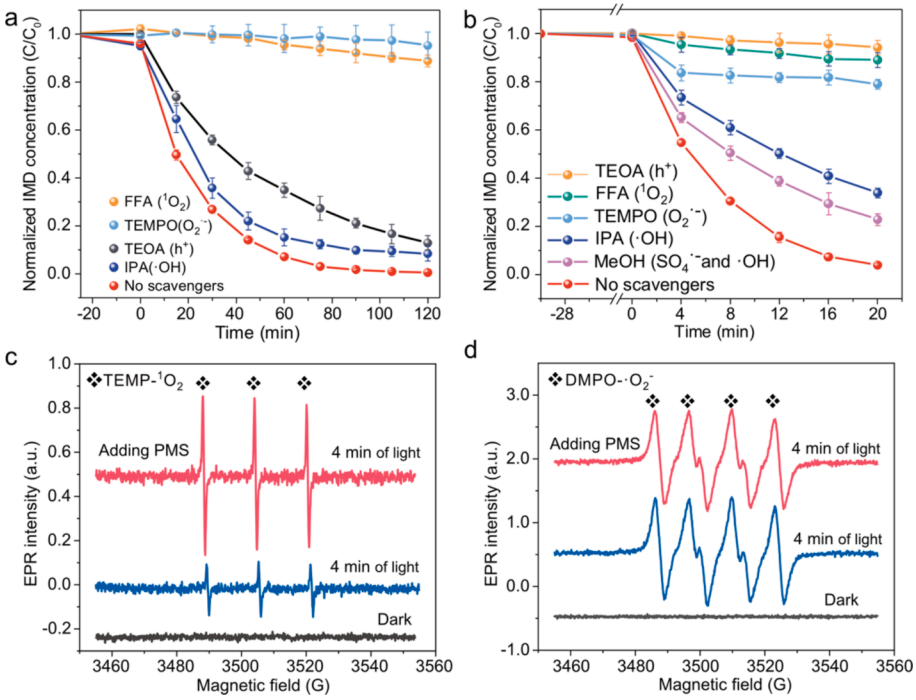

Fig. 6. The quenching experiments over HTCN vis PC system (a) and PC-PMS system (b); EPR spectra of $^1O_2$ (c) and $\bullet O_2^-$ (d) in the different processes.

degradation activity of HTCN is not very significant, and further optimization is needed in the future (see Tables S5 and S6 and Fig. S11). The superior activity of the HTCN photocatalyst results from the synergy of the ultrathin porous tubular architecture and the N_b vacancies. The ultrathin porous tubular architecture provides an ultrahigh-specific surface area and exposes abundant active sites, thereby ensuring efficient mass transfer and significantly reducing the diffusion distance of photogenerated carriers. In the meantime, the N_b vacancies serve as unsaturated sites, which hinder the recombination of photogenerated carriers and promote subsequent redox reactions. Cycling results in Fig. 5f show the excellent HTCN's reusability in IMD degradation, retaining its efficiency at 75.5 % after 10 cycles, and the XPS, XRD, and FTIR spectra of HTCN after degradation are almost identical to the pristine HTCN (Fig. S12). In addition, HTCN in the PC-PMS system has excellent anti-interference performance against variations in pH, water quality, and co-existing anions (Fig. S8d-f). The excellent stability of the HTCN is attributed to its stable graphite-like structure. Notably, HTCN's total organic carbon (TOC) removal rate for IMD can reach 38 % under 8 h of visible-light irradiation (Fig. S13a), which is consistent that the produced intermediates of IMD degradation gradually disappear with the extension of time of illumination (Fig. S13b). This analysis suggests the formation of small, non-UV-absorbing molecules like CO_2 and H_2O. Moreover, to evaluate the potential for large-scale practical application of the photocatalyst, a continuous custom-made photo-flow device was employed for IMD removal over three days. The schematic diagram of the device and experimental equipment is presented in Fig. S14a and S14b, respectively. The results show that almost no IMD was degraded using only outdoor sunlight (Fig. S14c). However, when both HTCN and PMS were added to the system, HTCN was able to remove up to 86 % of IMD during the 3-day continuous operation under sunlight. These results evidence the potential and competitiveness of HTCN as a non-metallic catalyst for IMD degradation.

3.6. Possible mechanism

To elucidate the mechanism behind the excellent degradation efficiency of IMD in the HTCN-driven PC-PMS system, we identified the reactive oxygen species (ROSs) generated that were responsible for the IMD degradation process using ROSs quenching experiments and EPR analysis. We used 1 mM of isopropyl alcohol (IPA) as the quenching agent of •OH, and 1 mM of methanol (MeOH) to eliminate both OH and $SO_4^{\bullet-}$, 1 mM triethanolamine (TEOA) for photogenerated holes (h^+), 1 mM of furfuryl alcohol (FFA) for $^1O_2$, and 1 mM of TEMPO for $\bullet O_2^-$[42–44]. We found that in the PC system, $^1O_2$ and $\bullet O_2^-$ are the main ROSs contributing to IMD degradation (Fig. 6a), where $\bullet O_2^-$ originates from the activation of O_2 molecules by photogenerated electron transfer, and $\bullet O_2^-$ can further react with photogenerated h^+ to produce $^1O_2$. The IMD degradation can also be achieved by blocking the conversion of $\bullet O_2^-$ to $^1O_2$ after trapping the photogenerated h^+, suggesting that IMD degradation can be achieved by $\bullet O_2^-$ alone. Hence, the photogenerated electrons in the PC system play a crucial role in the generation of $\bullet O_2^-$, but the photogenerated h^+ is not well utilized, resulting in waste. Conversely, in the PC-PMS system, photogenerated h^+, $^1O_2$, and $\bullet O_2^-$ all play significant roles in IMD degradation (Fig. 6b). Interestingly, the addition of PMS leads to the photogenerated h^+ towards IMD degradation, which is a considerable difference in the PC system where it plays a limited role. Therefore, we conclude that photogenerated h^+ are critical for PMS activation. As previously reported, this activation mainly generates $^1O_2$. Then, O_2^- in the PC-PMS system originates from the reduction of O_2 by photogenerated electrons, while $^1O_2$ arises from the oxidation of PMS by photogenerated h^+. The sustained release of $\bullet O_2^-$ and $^1O_2$ under these conditions enables HTCN to achieve complete imidacloprid degradation in the PC-PMS system.

EPR characterization using DMPO and TEMP as free radical spin trapping agents further confirmed ROS production in the PC-PMS system [45–47]. Notably, a characteristic TEMP -$^1O_2$ triple peak (1:1:1) was observed under light conditions (Fig. 6c), while this signal was barely detectable under dark conditions. Moreover, the TEMP-$^1O_2$ signal gets drastically enhanced when PMS is added, indicating that the generated $^1O_2$ can play a dominant role in the IMD degradation. ROS quenching experiments suggest that this $^1O_2$ is mainly generated by the oxidation of PMS by photogenerated h^+. As shown in Fig. 6d, a strong DMPO-$\bullet O_2^-$ quadruple characteristic peak (1:1:1:1) appears under light conditions. This signal remains largely unchanged with PMS addition, indicating that the $\bullet O_2^-$ production is primarily driven by O_2 reduction by photogenerated electrons, consistent with ROS quenching results.

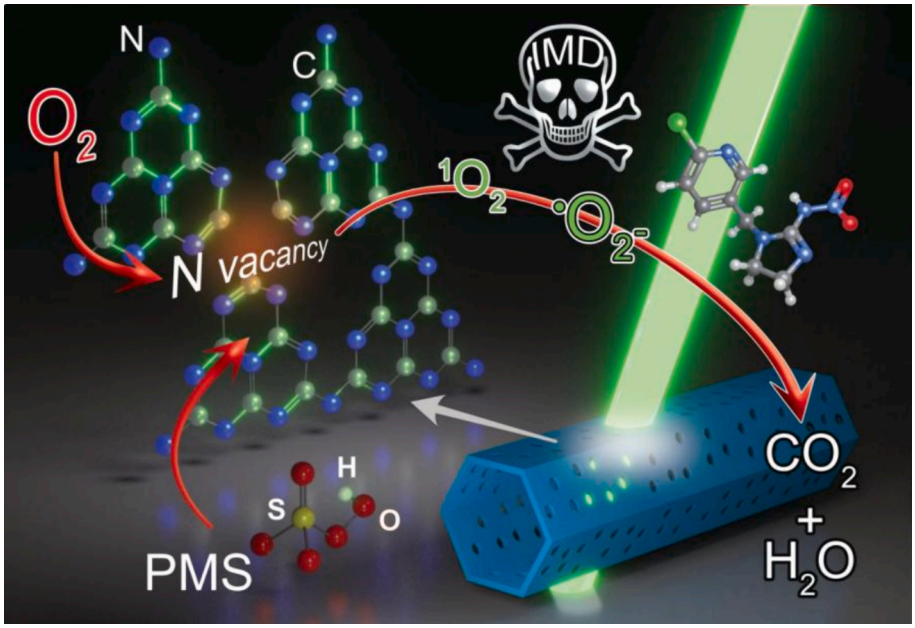

Fig. 7. Schematic illustration of the HTCN-driven PC-PMS system for imidacloprid degradation.

Accordingly, we calculated the Gibbs free energy change (ΔG) for each step involved in reducing O_2 to $\bullet O_2^-$ via photogenerated electrons, as shown in Fig. S16a and b. The rate-limiting step of TCN is the conversion of $*O_2$ to $*\bullet O_2^-$, which has an energy barrier of −0.65 eV. In contrast, the ΔG of HTCN for this decisive rate step is −8.54 eV. Therefore, the O_2 adsorbed on the active site of HTCN can be spontaneously converted to $\bullet O_2^-$ to favorably affect the subsequent site reactions. We also studied the PMS activation pathways involved in oxidizing PMS to $^1O_2$ via photogenerated holes (Fig. S17a and b). The energy barrier of 2.35 eV for PMS activation on TCN was too high, and the relative energy of the product is 2.13 eV. These results show that the activation of PMS on TCN is not a thermodynamically spontaneous process. Interestingly, the energy barrier of 0.87 eV for PMS activation on HCN is easier to overcome, and the relative energy of the product is −2.75 eV, indicating that the PMS activation is exothermic and can occur spontaneously under ambient conditions. Experiments and computations demonstrate that the full reaction photo-production of $\bullet O_2^-$ and $^1O_2$ that can combine O_2-reduction and PMS-oxidation is highly demanded to maximize the carries-utilization to remove the IMD contaminants in a PC-PMS system. In summarizing these results combined with electrostatic potential distribution (Fig. S15), we elucidated a possible mechanism in Fig. 7 for the improved IMD degradation efficiency in the HTCN-driven PC-PMS system.

In short, this work features several novelty points: 1) High-temperature H_2 was used to introduce three-coordinated nitrogen vacancies into g-C_3N_4 and realize efficient stripping of g-C_3N_4 tubes into an ultrathin porous tubular architecture. 2) Our HTCN shows superior IMD degradation in PC and PC-PMS systems compared to metrics reported in previous reports. 3) Our study achieves the full utilization of photogenerated electron-hole pairs conversion to $\bullet O_2^-$ and $^1O_2$ for the IMD's degradation through the precise structural design of g-C_3N_4 in the PC-PMS system.

4. Conclusion

In summary, we present a new strategy for fabricating ultrathin porous g-C_3N_4 tubes with N_b vacancies as a metal-free photocatalyst via H_2-assisted heat treatment. DFT calculations reveal the intricate interactions between H_2 molecules and the g-C_3N_4 framework, evidencing the stripping and perforating effects of H_2 molecules that resulted in the unique g-C_3N_4 ultrathin tube structure. We obtained optimized electronic properties, enhanced photogenerated carrier utilization, and enriched active sites by simultaneously engineering N_b vacancies and ultrathin porous architecture. The resultant HTCN photocatalyst exhibits excellent catalytic activity and stability for O_2 and PMS's conversion to $^1O_2$, and $\bullet O_2^-$, respectively. The main $\bullet O_2^-$ and $^1O_2$ in the system collectively achieve full IMD degradation within 20 min with superior reaction rate constant K (0.16 min^{-1}). The HTCN also presents a robust anti-interference ability under different reaction conditions and excellent recyclability, indicating its high universality and practical potential. This work offers significant insights for constructing novel metal-free photocatalysts for sustainable and efficient water pollution remediation driven by sunlight.

CRediT authorship contribution statement

Bin Yang: Writing – review & editing, Writing – original draft, Visualization, Validation, Supervision, Software, Resources, Project administration, Methodology, Investigation, Funding acquisition, Formal analysis, Data curation, Conceptualization. **Jiaojiao Zhao:** Writing – original draft, Investigation, Data curation. **Youpeng Xiong:** Software, Methodology. **Cuihua Li:** Writing – review & editing, Visualization. **Mei Zhang:** Writing – review & editing. **Raul D. Rodriguez:** Writing – review & editing, Visualization. **Xin Jia:** Writing – review & editing, Funding acquisition.

Declaration of competing interest

The authors declare that they have no known competing financial interests or personal relationships that could have appeared to influence the work reported in this paper.

Data availability

Data will be made available on request.

Acknowledgments

This study was mainly supported by the National Natural Science Foundation of China (Grant No. 22308223), the High-level Talents

launching Project (RCZK202328), and Xinjiang Uygur Autonomous Region Tianchi Talent Introduction Program (Young Doctor) for Bin Yang. This study was also supported by the National Natural Science Foundation of China (Grant No. U1703351, 52073179), Tiansh an Talent Support Program for Xin Jia, and the Program of Introducing Talents of Discipline to Universities (D20018). RDR acknowledges the Agrochemical Engineering Innovation and Intelligence Base for Oasis Ecology.

Appendix A. Supplementary data

Supplementary data to this article can be found online at https://doi.org/10.1016/j.cej.2024.155117.

References

[1] K. Yin, Y. Deng, C. Liu, Q. He, Y. Wei, S. Chen, T. Liu, S. Luo, Kinetics, pathways and toxicity evaluation of neonicotinoid insecticides degradation via UV/chlorine process, Chem. Eng. J. 346 (2018) 298–306.
[2] F. Martelli, Z. Zhongyuan, J. Wang, C.-O. Wong, N.E. Karagas, U. Roessner, T. Rupasinghe, K. Venkatachalam, T. Perry, H.J. Bellen, P. Batterham, Low doses of the neonicotinoid insecticide imidacloprid induce ROS triggering neurological and metabolic impairments in Drosophila [Neuroscience], Proc. Natl. Acad. Sci. u.s.a. 117 (2020) 25840–25850.
[3] X. Wang, D. Goulson, L. Chen, J. Zhang, W. Zhao, Y. Jin, S. Yang, Y. Li, J. Zhou, Occurrence of neonicotinoids in Chinese apiculture and a corresponding risk exposure assessment, Environ. Sci. Technol. 54 (2020) 5021–5030.
[4] X. Xu, Y. Sui, W. Chen, W. Huang, X. Li, Y. Li, D. Liu, S. Gao, W. Wu, C. Pan, H. Zhong, H. Wen, M. Wen, The photocatalytic H_2O_2 production by metal-free photocatalysts under visible-light irradiation, Appl. Catal. b: Environ. 341 (2024) 123271.
[5] L. Di, T. Wang, Q. Lu, J. Lu, Y. Zhang, Y. Zhou, Y. Zhou, Efficient PMS activation toward degradation of bisphenol A by metal-free nitrogen-doped hollow carbon spheres, Sep. Purif. Technol. 339 (2024) 126740.
[6] W. Cheng, H. Liu, G. Liao, R. Wang, X. Zhao, L. Zhou, R.D. Rodriguez, B. Yang, X. Jia, Directional charge transfer modulation in ultrathin polyporous carbon nitride nanotubes for enhanced peroxymonosulfate activation, Carbon 222 (2024) 118977.
[7] M. Qian, X.-L. Wu, M. Lu, L. Huang, W. Li, H. Lin, J. Chen, S. Wang, X. Duan, Modulation of charge trapping by island-like single-atom cobalt catalyst for enhanced photo-fenton-like reaction, Adv. Funct. Mater. 33 (2023) 2208688.
[8] Q. Wen, D. Li, H. Li, M. Long, C. Gao, L. Wu, F. Song, J. Zhou, Synergetic effect of photocatalysis and peroxymonosulfate activated by Co/Mn-MOF-74@g-C_3N_4 Z-scheme photocatalyst for removal of tetracycline hydrochloride, Sep. Purif. Technol. 313 (2023) 123518.
[9] P. Qiu, Z. Cheng, N. Xue, Y. Zeng, X. Kai, S. Zhang, C. Xu, F. Liu, Z. Guo, The synergistic effect in metal-free graphene oxide coupled graphitic carbon nitride/light/peroxymonosulfate system: Photothermal effect and catalyst stability, Carbon 178 (2021) 81–91.
[10] Y. Yang, X. Li, C. Zhou, W. Xiong, G. Zeng, D. Huang, C. Zhang, W. Wang, B. Song, X. Tang, X. Li, H. Guo, Recent advances in application of graphitic carbon nitride-based catalysts for degrading organic contaminants in water through advanced oxidation processes beyond photocatalysis: A critical review, Water Res. 184 (2020) 116200.
[11] V. Hasija, V.-H. Nguyen, A. Kumar, P. Raizada, V. Krishnan, A.A.P. Khan, P. Singh, E. Lichtfouse, C. Wang, P. Thi Huong, Advanced activation of persulfate by polymeric g-C_3N_4 based photocatalysts for environmental remediation: A review, J. Hazard. Mater. 413 (2021) 125324.
[12] G. Liao, Y. Gong, L. Zhang, H. Gao, G.-J. Yang, B. Fang, Semiconductor polymeric graphitic carbon nitride photocatalysts: the “holy grail” for the photocatalytic hydrogen evolution reaction under visible light, Energy Environ. Sci. 12 (2019) 2080–2147.
[13] B. Yang, J. Han, Q. Zhang, G. Liao, W. Cheng, G. Ge, J. Liu, X. Yang, R. Wang, X. Jia, Carbon defective g-C_3N_4 thin-wall tubes for drastic improvement of photocatalytic H_2 production, Carbon 202 (2023) 348–357.
[14] B. Yang, Z. Wang, J. Zhao, X. Sun, R. Wang, G. Liao, X. Jia, 1D/2D carbon-doped nanowire/ultra-thin nanosheet g-C_3N_4 isotype heterojunction for effective and durable photocatalytic H_2 evolution, Int. J. Hydrogen Energy 46 (2021) 25436–25447.
[15] J. Zhou, T. Shan, F. Zhang, B. Boury, L. Huang, Y. Yang, G. Liao, H. Xiao, L. Chen, A novel dual-channel carbon nitride homojunction with nanofibrous carbon for significantly boosting photocatalytic hydrogen peroxide production, Adv. Fiber Mater. 6 (2024) 387–400.
[16] C. Li, H. Lu, G. Ding, Q. Li, G. Liao, Recent advances on g-C_3N_4-based Z-scheme photocatalysts for organic pollutant removal, Catal Sci. Technol. 13 (2023) 2877–2898.
[17] B. Wu, L. Zhang, B. Jiang, Q. Li, C. Tian, Y. Xie, W. Li, H. Fu, Inside back cover: ultrathin porous carbon nitride bundles with an adjustable energy band structure toward simultaneous solar photocatalytic water splitting and selective phenylcarbinol oxidation, Angew. Chem. Int. Ed. 60 (2021) 4951.
[18] S. Guo, Z. Deng, M. Li, B. Jiang, C. Tian, Q. Pan, H. Fu, Phosphorus-doped carbon nitride tubes with a layered micro-nanostructure for enhanced visible-light photocatalytic hydrogen evolution, Angew. Chem. Int. Ed. 55 (2016) 1830–1834.
[19] Q. Li, Y. Jiao, Y. Tang, J. Zhou, B. Wu, B. Jiang, H. Fu, Shear stress triggers ultrathin-nanosheet carbon nitride assembly for photocatalytic H_2O_2 production coupled with selective alcohol oxidation, J. Am. Chem. Soc. 145 (2023) 20837–20848.
[20] Y. Xiao, G. Tian, W. Li, Y. Xie, B. Jiang, C. Tian, D. Zhao, H. Fu, Molecule self-assembly synthesis of porous few-layer carbon nitride for highly efficient photoredox catalysis, J. Am. Chem. Soc. 141 (2019) 2508–2515.
[21] G. Ge, X. Guo, C. Song, Z. Zhao, Reconstructing supramolecular aggregates to nitrogen-deficient g-C3N4 bunchy tubes with enhanced photocatalysis for H_2 production, ACS Appl. Mater. Interfaces 10 (2018) 18746–18753.
[22] Y. Zhang, J. Di, P. Ding, J. Zhao, K. Gu, X. Chen, C. Yan, S. Yin, J. Xia, H. Li, Ultrathin g-C_3N_4 with enriched surface carbon vacancies enables highly efficient photocatalytic nitrogen fixation, J. Colloid Interface Sci. 553 (2019) 530–539.
[23] Y. Wang, L. Rao, P. Wang, Y. Guo, Z. Shi, X. Guo, L. Zhang, Synthesis of nitrogen vacancies g-C_3N_4 with increased crystallinity under the controlling of oxalyl dihydrazide: Visible-light-driven photocatalytic activity, Appl. Surf. Sci. 505 (2020) 144576.
[24] J. Wu, N. Li, H.-B. Fang, X. Li, Y.-Z. Zheng, X. Tao, Nitrogen vacancies modified graphitic carbon nitride: scalable and one-step fabrication with efficient visible-light-driven hydrogen evolution, Chem. Eng. J. 358 (2019) 20–29.
[25] L. Chen, H. Li, H. Li, H. Li, W. Qi, Q. Zhang, J. Zhu, P. Zhao, S. Yang, Accelerating photogenerated charge kinetics via the g-C_3N_4 Schottky junction for enhanced visible-light-driven CO_2 reduction, Appl. Catal. B Environ. Energy 318 (2022) 121863.
[26] Y. Li, Z. He, L. Liu, Y. Jiang, W.-J. Ong, Y. Duan, W. Ho, F. Dong, Inside-and-out modification of graphitic carbon nitride (g-C_3N_4) photocatalysts via defect engineering for energy and environmental science, Nano Energy 105 (2023) 108032.
[27] X. Zhu, Y. Jia, Y. Liu, J. Xu, H. He, S. Wang, Y. Shao, Y. Zhai, Y. Zhu, Enhancing built-in electric fields via molecular symmetry modulation in supramolecular photocatalysts for highly efficient photocatalytic hydrogen evolution, Angew. Chem. Int. Ed. 63 (2024) e202405962.
[28] Y. Xue, C. Ma, Q. Yang, X. Wang, S. An, X. Zhang, J. Tian, Construction of g-C_3N_4 with three coordinated nitrogen (N_3C) vacancies for excellent photocatalytic activities of N_2 fixation and H_2O_2 production, Chem. Eng. J. 457 (2023) 141146.
[29] Z. Jiang, X. Zhang, H. Chen, P. Yang, S. Jiang, Fusiform-shaped g-C_3N_4 capsules with superior photocatalytic activity, Small 16 (2020) 2003910.
[30] G. Dong, D.L. Jacobs, L. Zang, C. Wang, Carbon vacancy regulated photoreduction of NO to N_2 over ultrathin g-C_3N_4 nanosheets, Appl. Catal. B Environ. Energy 218 (2017) 515–524.
[31] B. Yang, X. Li, Q. Zhang, X. Yang, J. Wan, G. Liao, J. Zhao, R. Wang, J. Liu, R. D. Rodriguez, X. Jia, Ultrathin porous carbon nitride nanosheets with well-tuned band structures via carbon vacancies and oxygen doping for significantly boosting H_2 production, Appl. Catal. B Environ. Energy 314 (2022) 121521.
[32] W. Li, Z. Wei, K. Zhu, W. Wei, J. Yang, J. Jing, D.L. Phillips, Y. Zhu, Nitrogen-defect induced trap states steering electron-hole migration in graphite carbon nitride, Appl. Catal. B Environ. Energy 306 (2022) 121142.
[33] Y. Zhu, J. Ren, G. Huang, C.-L. Dong, Y.-C. Huang, P. Lu, H. Tang, Y. Liu, S. Shen, D. Yang, Red phosphorus grafted high-index (116) faceted anatase TiO_2 for Z-scheme photocatalytic pure water splitting, Adv. Funct. Mater. 34 (2024) 2311623.
[34] Y. Hong, C. Li, Z. Fang, B. Luo, W. Shi, Rational synthesis of ultrathin graphitic carbon nitride nanosheets for efficient photocatalytic hydrogen evolution, Carbon 121 (2017) 463–471.
[35] D. Zhao, C. Dong, B. Wang, C. Chen, Y. Huang, Z. Diao, S. Li, L. Guo, S. Shen, Synergy of dopants and defects in graphitic carbon nitride with exceptionally modulated band structures for efficient photocatalytic oxygen evolution, Adv. Mater. 31 (2019) 1903545.
[36] N.P. Dharmarajan, M. Fawaz, C. Sathish, S.N. Talapaneni, K. Ramadass, A. M. Sadanandan, X.M.C. Ta, M. Huš, V. Perumalsamy, A. Tricoli, B. Likozar, C. Jeon, J. Yang, A. Vinu, Insights into atomic level π-electron modulations in supramolecular carbon nitride nanoarchitectonics for sustainable green hydrogen production, Adv. Energy Mater. (2024) 2400686. Early View.
[37] Z. Wang, G. Ding, J. Zhang, X. Lv, P. Wang, L. Shuai, C. Li, Y. Ni, G. Liao, Correction: Critical role of hydrogen bonding between microcrystalline cellulose and g-C_3N_4 enables highly efficient photocatalysis, Chem. Commun. 60 (2024) 1193.
[38] J. Xu, L. Zhang, R. Shi, Y. Zhu, Chemical exfoliation of graphitic carbon nitride for efficient heterogeneous photocatalysis, J. Mater. Chem. A 1 (2013) 14766–14772.
[39] J. Yi, T. Fei, L. Li, Q. Yu, S. Zhang, Y. Song, J. Lian, X. Zhu, J. Deng, H. Xu, H. Li, Large-scale production of ultrathin carbon nitride-based photocatalysts for high-yield hydrogen evolution, Appl. Catal. B Environ. Energy 281 (2021) 119475.
[40] B. Yang, J. Zheng, W. Li, R. Wang, D. Li, X. Guo, R.D. Rodriguez, X. Jia, Engineering Z-scheme TiO_2-OV-BiOCl via oxygen vacancy for enhanced photocatalytic degradation of imidacloprid, Dalton Trans. 49 (2020) 11010–11018.
[41] T. Shan, J. Li, S. Wu, H. Wu, F. Zhang, G. Liao, H. Xiao, L. Huang, L. Chen, Boosting H_2O_2 production over carboxymethyl cellulose modified g-C_3N_4 via hydrogen-bonding-assisted charge transfer, Chem. Eng. J. 478 (2023) 147509.
[42] H. Liu, Y. Fu, S. Chen, W. Zhang, K. Xiang, F. Shen, R. Xiao, L. Chai, F. Zhao, A layered g-C_3N_4 support Single-Atom Fe-N4 catalyst derived from hemin to Activate PMS for Selective degradation of electron-rich compounds via singlet oxygen species, Chem. Eng. J. 474 (2023) 145571.

[43] L. Jing, M. Xie, Y. Xu, C. Tong, X. Du, H. Zhao, N. Zhong, H. Li, J. Hu, Advanced oxidation via the synergy of C-defective/ C-O band modified ultrathin porous g-C_3N_4 and PMS for efficient photothermal degradation of bisphenol pollutants and lignin derivatives, Green, Energy Environ. (2023) 1159–1170.
[44] Z. Weng, Y. Lin, B. Han, X. Zhang, Q. Guo, Y. Luo, X. Ou, Y. Zhou, J. Jiang, Donor-acceptor engineered g-C_3N_4 enabling peroxymonosulfate photocatalytic conversion to $^1O_2$ with nearly 100% selectivity, J. Hazard. Mater. 448 (2023) 130869.
[45] Z. Chen, T. Li, Y. Zhu, X. Liang, Z. Zhao, D. Wang, J. Li, Y. Gao, C. Hu, Efficient light-free activation of peroxymonosulfate by carbon ring conjugated carbon nitride for elimination of organic pollutants, Chem. Eng. J. 420 (2021) 129671.
[46] Y. Shi, J. Li, D. Wan, J. Huang, Y. Liu, Peroxymonosulfate-enhanced photocatalysis by carbonyl-modified g-C_3N_4 for effective degradation of the tetracycline hydrochloride, Sci. Total Environ. 749 (2020) 142313.
[47] X. Wang, J. Jiang, Y. Ma, Y. Song, T. Li, S. Dong, Tetracycline hydrochloride degradation over manganese cobaltate ($MnCo_2O_4$) modified ultrathin graphitic carbon nitride (g-C_3N_4) nanosheet through the highly efficient activation of peroxymonosulfate under visible light irradiation, J. Colloid Interface Sci. 600 (2021) 449–462.